Does Cavitation Affect Droplet Breakup in High-Pressure Homogenization? Insights into Local Effects

Felix Johannes Preiss*, Maximilian Hetz, and Heike Petra Karbstein[‡]

DOI: 10.1002/cite.202100104

This is an open access article under the terms of the Creative Commons Attribution License, which permits use, distribution and reproduction in any medium, provided the original work is properly cited.

Dedicated to Prof. Dr. Thomas Hirth on the occasion of his 60th birthday

High-pressure homogenization is a popular method to produce emulsions of droplet sizes smaller than 1 µm. Regarding the role of cavitation in the process, it is still discussed controversially whether it promotes or hinders droplet breakup during high-pressure homogenization. In this study droplet breakup in a cavitating flow of an optically accessible high-pressure homogenizer orifice is visualized using a high-speed camera setup. The cavitation regime is characterized using laser light induced luminescence. Droplet deformation and breakup events are compared to a cavitation-free flow with the same specific energy input. Once the jet cavitation regime is reached, droplet breakup took place further downstream the orifice exit, and the larger droplets are measured in the final product.

Keywords: Cavitation, Droplet breakup, High-pressure homogenization, Orifice

Received: June 10, 2021; *revised:* July 16, 2021; *accepted:* July 20, 2021

1 Introduction

High-pressure homogenization is a commonly used process to produce emulsions of a low to medium viscosity and droplet sizes of less than 1 µm. During the process, a pre-emulsion with large droplets is pumped with a pressure of several hundred bar through a disruption unit, where the flow is accelerated due to the reduction of the cross section of the flow channel. The disruption unit can be designed as flat valves or orifices in manifold variations. When the droplets in the pre-emulsion are accelerated whilst entering the disruption unit, they are exposed to shear forces and elongation strain, which results in a deformation to thin threads [1, 2]. In the outlet channel of the disruption unit a free jet is formed. In the core area of the free jet, the velocity stays constant and thus the deformed droplets are force-free, which can result in a partially relaxation. The core area is surrounded by a shear layer where vortex structures are formed by the velocity gradient between the jet and the ambient fluid. The shear layer thickness increases with increasing distance from the orifice exit and the jet is spreading by the entrainment of the ambient fluid [3]. The first large high-energy vortex decay to smaller less intense vortex until the energy is dissipated in heat [4, 5]. The highly stretched droplets are subjected to viscous and/or inertial stresses depending on the flow path, leading to breakup into many small fragments [6]. When the static pressure in the orifice entrance drops below the vapor pressure of the fluid cavitation, bubbles are formed which follow the flow, continuing to grow [7]. This may have different effects: On the one hand, cavitation bubbles change local flow conditions and the resulting local stresses and thus, the stress history of the filaments. On the other hand, the implosion of cavitation bubbles causes microjets [8], which trigger very high stresses in the immediate vicinity. It is not surprising, therefore, that the influence of cavitation on the emulsification result in high-pressure homogenizers is discussed very controversially in literature [9].

Previous investigations have shown that emulsions with larger droplets are formed if severe cavitation is present [10–13]. Other authors consider the effect of the imploding cavitation bubbles to be the main reason for the efficient droplet breakup in high-pressure homogenizers [14].

Several authors have investigated cavitation patterns in and downstream of orifices in more detail [15–19], so that four cavitation regimes can be distinguished. At cavitation inception unstable bubble growth takes place and first gas bubbles are visible in the outlet channel [20]. The inception

Felix Johannes Preiss, Maximilian Hetz,
Prof. Dr.-Ing. Heike Petra Karbstein
felix.preiss@kit.edu
Karlsruhe Institute of Technology (KIT), Institute of Process Engineering in Life Sciences, Food Process Engineering, Kaiserstraße 12, 76131 Karlsruhe, Germany.
[‡]formerly Schuchmann.

 © 2021 The Authors. Chemie Ingenieur Technik published by Wiley-VCH GmbH

15222640, 2022, 3, Downloaded from https://onlinelibrary.wiley.com/doi/10.1002/cite.202100104 by Karlsruher Inst F. Technologie, Wiley Online Library on [21/10/2022]. See the Terms and Conditions (https://onlinelibrary.wiley.com/terms-and-conditions) on Wiley Online Library for rules of use; OA articles are governed by the applicable Creative Commons License

of cavitation can also be affected by pseudo cavitation in which case gases dissolved in the fluid at ambient pressure are released if the static pressure in the flow decreases [21]. Jet cavitation is present when the static pressure drops below the vapor pressure of the fluid. First vapor bubbles are formed at the inlet of the orifice and transported to the outlet channel, where they collapse [22]. The cavitation jet is disrupted periodically due to the periodical detachment of the flow in the orifice wall [23]. This behavior is also called cavitation shedding. If a coherent cavitation vapor bubble is formed in the outlet channel, the cavitation regime is called choked cavitation [24]. A hydraulic flip is present if the cavitation bubble completely sheathes the fluid jet in the outlet channel and thus the jet is completely detached from the outlet channel wall [23].

The production of cavitation bubbles can be reduced or even completely impeded by applying a backpressure at the outlet as first shown by McKillop et al. [25]. When applying about 30 % to 50 % of the inlet pressure as backpressure, depending on the geometry of the flow channel, the cavitation can be suppressed. The ratio of backpressure p_{bp} in the outlet to inlet pressure p_{in} is described as the Thoma number Th [26].

$$Th = p_{bp}/p_{in} \tag{1}$$

The Thoma number cannot predict the presence of cavitation at low inlet pressures if, e.g., only ambient pressure is applied at the outlet [10]. The cavitation number σ allows to forecast the production of cavitation bubbles at low pressures. According to Gothsch et al. [16] it is defined to

$$\sigma = \frac{p_{in} - p_{bp}}{p_{bp} - p_v} \tag{2}$$

where p_v is the vapor pressure of the continuous phase.

The flow regime in the orifice is characterized with the Reynolds number Re.

$$Re = \frac{\bar{u} D \rho}{\eta} \tag{3}$$

Where $\bar{u}$ is the average velocity in the orifice, which can be calculated with the experimentally measured mass flow, D is the orifice diameter, ρ the density of the used fluid and η is the dynamic viscosity of the fluid.

The aim of this work is to give more insights in the effect of cavitation on droplet deformation and breakup, concentrating on local effects in the free jet in order to increase mechanistic understanding of the effect of cavitation on high-pressure homogenizing results. This will allow optimizing the geometry of high-pressure disruption units and transferring this knowledge to industrial scales.

2 Materials and Methods

2.1 Principle Approach

In this investigation, an orifice will be used as model disruption unit, due to better optical accessibility compared to a flat valve. Droplet breakup phenomena during high-pressure homogenization in a cavitating flow will be compared with the droplet breakup phenomena in a cavitation-free flow at the same pressure loss by applying a backpressure. To visualize the cavitation pattern, a fluorescence dye is added to the continuous phase and images of the flow in the optically accessible outlet flow channel are taken with a high-speed camera setup alike the method of Gothsch et al. [16]. Subsequently, the droplet breakup is visualized with fluorescence labeled oil droplets with the same high-speed camera setup as described in [1, 27, 28].

2.2 Materials

To visualize the cavitation in the process, 6 ppm of the water-soluble fluorescence dye Rhodamine B (VWR International GmbH, Bruchsal, Germany) is solved in the continuous phase.

The continuous phase for the droplet visualization experiment consists of demineralized water and 0.01233 wt % polysorbate 20 (Tween 20®, Carl Roth, Karlsruhe, Germany). The Tween 20 concentration equals the double of the critical micelle concentration (CMC) [29] to ensure that the pre-emulsion is stable prior to the droplet breakup and that the same cavitation regime is present, as this can be influenced by the emulsifier concentration [11]. The same emulsifier concentration is also used later for the visualization of the droplet breakup events. The influence of ingredients like dye and emulsifier on the vapor pressure is neglected in this present article. A water vapor pressure of p_v (20 °C) = 0.02347 bar [30] is used for all calculations in this investigation.

A mixture of a middle-chain-triglyceride oil (Miglyol 840®, IOI Oleo GmbH, Witten, Germany) and 120 ppm Nile red dye (9-(diethyl-amino)benzo[a]phenoxazin-5(5H)-one, Sigma-Aldrich Chemie GmbH, St. Louis, MO, USA) is used as disperse phase.

The pre-emulsion is made from 5 wt % colored oil, 0.5 wt % Tween 20 and 94.5 wt % demineralized water with a Disperser T25 Ultra-Turrax® (IKA®-Werke GmbH & Co. KG, Staufen, Germany) at 1200 min^{-1} for 10 min. In the next step, a diluted pre-emulsion is made by mixing 0.25 wt % of the pre-emulsion with 99.75 wt % of the continuous phase. This results in a disperse phase fraction of 0.0125 wt %. The droplet size distribution of the pre-emulsion has a median droplet size of $d_{50,3}$ = 44.77 ± 0.60 µm.

For measurements of the resulting droplet size distribution, the experiments were repeated with the continuous phase consisting of 99.5 wt % demineralized water and 0.5 wt % polysorbate 20 (Tween 20®, Carl Roth, Karlsruhe,

 © 2021 The Authors. Chemie Ingenieur Technik published by Wiley-VCH GmbH

15222640, 2022, 3, Downloaded from https://onlinelibrary.wiley.com/doi/10.1002/cite.202100104 by Karlsruher Inst F. Technologie, Wiley Online Library on [21/10/2022]. See the Terms and Conditions (https://onlinelibrary.wiley.com/terms-and-conditions) on Wiley Online Library for rules of use; OA articles are governed by the applicable Creative Commons License

Germany) and the previously described disperse phase. The increased emulsifier concentration ensures that all droplets are stabilized after the breakup in the orifice. The pre-emulsion is made with the same procedure except for the diluted pre-emulsion being made of 20 wt % pre-emulsion and 80 wt % continuous phase, which results in a disperse phase fraction of 1 wt %. This allows measurements by laser diffraction analysis.

The dynamic viscosity of the disperse phase is measured with a rotational rheometer (Anton Paar Physica MCR 101, Graz, Austria) at a temperature of 20 °C to 0.0101 Pa s with Newtonian flow behavior. An OCA 15 LJ (DataPhysics Instruments GmbH, Filderstadt, Germany) is used to determine the interfacial tension between the continuous and the disperse phase. The interfacial tension was identified as being 3.7 mN m^{-1} after a measuring time of 2 h at a temperature of 20 °C. An overview of all material properties can be found in Tab. 1.

Table 1. Overview of material properties (20 °C).

	Viscosity [Pa s]	Density [kg m^{-3}]
Disperse phase	0.0101	930[a)]
Continuous phase	0.000890 [31]	999.975 [32]

a) According to suppliers' information.

In order to properly represent the industrial conditions, all phases are not degassed prior to processing in the test rig. It is expected that pseudo cavitation may appear and be superimposed with normal cavitation.

2.3 Experimental Setup

The experimental setup is depicted in Fig. 1. The colored continuous phase is stored in a pressure vessel (b), which is pressurized by a nitrogen gas cylinder (a). This allows a pulsating free flow through the optically accessible orifice (e). A filter prohibits the blocking of the orifice with dirt particles. Pressures before and after the orifice are recorded during the experiment. When visualizing the cavitation, the needle valve (h), the pipe coil (d) and the sample collection hose (f) are demounted. The mass flow is determined by a continuous readout of a scale.

When performing droplet breakup visualization and measurements of the resulting droplet size distribution, the experimental setup with all components as shown in Fig. 1 is used. The diluted pre-emulsion is stored in a beaker (c). When the process conditions are in steady state, the valve of the pressure vessel is closed, and the diluted pre-emulsion is filled in a pipe coil (d). Following the reopening of the pressure vessel valve, the diluted pre-emulsion is pumped through the orifice. When measuring the resulting droplet size distribution, a sample is collected by emptying the hose (f) and subsequently analyzed using a laser light diffraction spectrometer including polarization intensity differential scattering (LS 13320® Beckman-Coulter, Brea, CA, USA). Again, the needle valve (h) is demounted if no backpressure should be applied.

The optically accessible orifice is milled in a stainless-steel block. The flow channel is covered with an acrylic glass plate to gain an optically accessible inlet and outlet channel. The square inlet channel has an edge length D_{in} of 2 mm. The outlet channel has a dimension of 3 mm × 3 mm where the edge length is defined as D_{exit}. A conical inlet with an angle $\alpha = 60°$ is positioned prior to the round orifice drilling hole with a diameter D of 0.2 mm. The drilling hole has a length L of 0.4 mm. To achieve a coaxial alignment of the

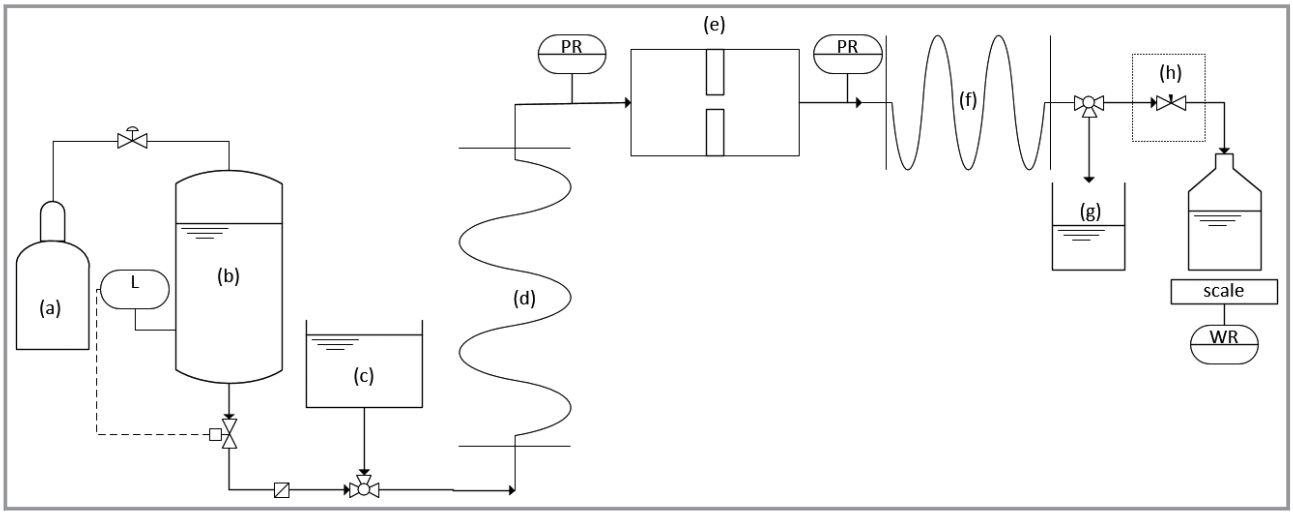

Figure 1. Experimental setup for cavitation visualization, droplet breakup visualization and determination of the resulting droplet size distribution.

 © 2021 The Authors. Chemie Ingenieur Technik published by Wiley-VCH GmbH

15222640, 2022, 3, Downloaded from https://onlinelibrary.wiley.com/doi/10.1002/cite.202100104 by Karlsruher Inst F. Technologie, Wiley Online Library on [21/10/2022]. See the Terms and Conditions (https://onlinelibrary.wiley.com/terms-and-conditions) on Wiley Online Library for rules of use; OA articles are governed by the applicable Creative Commons License

orifice to the outlet channel, the inlet channel is lowered by D_c = 0.5 mm, which is compensated by a protruding bar in the acrylic glass plate fitting the inlet channel. A sketch of the used orifice with all relevant dimensions is depicted in Fig. 2.

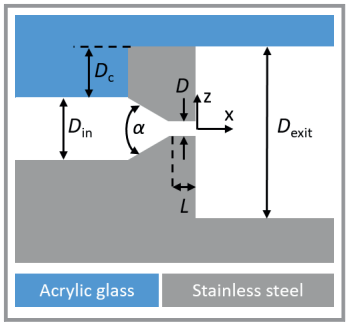

Figure 2. Cross section view of the optically accessible orifice.

The applied process parameters for droplet visualization are summarized in Tab. 2. Four pressure loss levels were used within the range from 10 bar to 50 bar. Higher pressure losses could not be achieved due to the limited pressure resistance of the optical accessible orifice. The Thoma number was either set to about 0.3 for a cavitation-free flow or to the minimal possible value at the used pressure loss for a cavitating flow. This resulted in cavitation number of about 2.2 for the cavitation-free flow and in a range of $17 \leq \sigma \leq 89$ for the cavitating flow. The used pressure losses led to Reynolds numbers within the range $916 \cdot 10^1$ to $383 \cdot 10^2$, which correspond to fully turbulent flow.

Table 2. Process parameters applied for droplet visualization.

Δp [bar]	σ [–]	Th [–]	Re [–]
9.5	17	0.058	$916 \cdot 10^1$
19.5	35	0.029	$131 \cdot 10^2$
29.5	54	0.019	$165 \cdot 10^2$
49.5	89	0.012	$247 \cdot 10^2$
9.2	2.2	0.32	$973 \cdot 10^1$
19.8	2.2	0.31	$142 \cdot 10^2$
29.2	2.2	0.31	$185 \cdot 10^2$
50.9	2.5	0.29	$383 \cdot 10^2$

2.4 Cavitation Visualization

The colored water phase is filled in the pressure vessel and pumped through the test rig at different pressure losses over the orifice with and without applied backpressure. The inlet and outlet pressure as well as the mass flow are recorded continuously during the experiment. The high-speed double frame camera and laser of a Dantec micro particle image velocimetry measurement (μ-PIV) are used to visualize the cavitation in this process. The setup consists of a CCD camera (FlowSense 4M Camera Kit, Dantec Dynamics, Skovlunde, Denmark) with a 12-bit resolution and 2048 × 2048 pixels, which is mounted to a microscope (Dantec HiPerformance Microscope, Skovlunde, Denmark). A resulting magnification of 5× is achieved with a 0.5× camera adapter in combination with a 10× magnification objective lens (C PLAN, Leica Microsystems Wetzlar GmbH, Wetzlar, Germany). A light guide is used to conduct the laser beam of the double-pulsed neodymium-doped yttrium aluminum garnet (ND:YAG) laser (Dual-Power 30-15 of Dantec Dynamics, Skovlunde, Denmark) through the microscope into the optically accessible orifice. This setup results in a visible area of $3 \times 3\ mm^2$ with a spatial resolution of 1.5 μm/px in the orifice channel. As the field of view does not cover the whole outlet channel, images of several sections with a displacement of 1 mm are taken and superimposed in the post-processing step. 2000 double images are taken for every section. One representative image is manually chosen for every section. Areas with higher dye concentrations representing liquid areas are colored brighter in the raw image. Areas with cavitation have a lower dye concentration and thus appear darker in the raw image. For better visibility, the contrast is adjusted, and the image is inverted. Therefore, areas with cavitation are shown as brighter pixels in the processed superimposed image.

2.5 Droplet Breakup Visualization

For droplet visualization, the continuous phase is run through the test rig until a steady state with the required pressure loss is reached. Subsequently, the valve of the pressure vessel is closed and about 200 mL of the diluted pre-emulsion are filled from the beaker (c) into the pipe coil (d). The valve is reopened afterwards, and the diluted pre-emulsion is pumped through the optically accessible orifice. Depending on the flow velocity, between 800 and 2000 double images of the outlet channel are taken at a frequency of 7.4 Hz with the previously described high-speed camera system. The time between the two images of the double image is set to 10 μs to be able to evaluate the evolution of the droplet deformation during the breakup process. Similar to the procedure of the cavitation visualization, images of several sections are taken. The commercial software Dynamic Studio 6.10 (Dantec Dynamics, Skovlunde, Denmark) is used to calculate an average image of all images of one experimental run, which is then subtracted from the single images to reduce the background noise. After exporting the images, all further image processing is made with MATLAB 2019b (Mathworks, Nantucket, MA, USA). The images are transformed to binary images and followed by that, objects with less than 200 pixel or a circularity c greater than 0.7 (a perfect circle has a circularity c = 1) are removed from the image, as these objects can be identified as noise or droplets that are relaxed to spheres in the backflow area around the jet. As the droplets are exposed to high stresses

 © 2021 The Authors. Chemie Ingenieur Technik published by Wiley-VCH GmbH

15222640, 2022, 3, Downloaded from https://onlinelibrary.wiley.com/doi/10.1002/cite.202100104 by Karlsruher Inst F. Technologie, Wiley Online Library on [21/10/2022]. See the Terms and Conditions (https://onlinelibrary.wiley.com/terms-and-conditions) on Wiley Online Library for rules of use; OA articles are governed by the applicable Creative Commons License

in the inlet of the orifice as presented in [1], all droplets with a size above the spatial resolution limit are expected to be deformed distinctly. Very small droplets might pass the orifice only slightly deformed, or they might relax to spheres before entering the shear layer of the jet. Nevertheless, as these small droplets either cannot be visualized with the used setup due to the spatial resolution limit or cannot be distinguished from the pronounced camera sensor noise, they are not taken into account for this investigation. In the next step, a criterion *crit* is established to describe the droplet deformation.

$$crit = (c + e)/2 \tag{4}$$

The extent e describes the ratio of the pixel of the object to the pixel of the bounding box of the object. Only droplets with an empirical value $crit < 0.42$ are considered further, as droplets that fulfill this criterion were found to be deformed droplets (small c value) or droplets that are in the droplet breakup process (small e value). Droplets that are out of the focus plane are sometimes depicted as porous objects, which are eliminated in the next step by removing all objects that have a porosity greater than 0.8, whereby the porosity is defined as the ratio of pixel number of the object to the pixel number of the object when all pores are closed. All remaining droplets are assumed to be correctly depicted droplets in the jet. In the figures a minimum of 68 single droplets were superimposed to depict effects in the droplet population. Representative droplets are displayed enlarged individually.

2.6 Determination of the Resulting Droplet Size Distribution

To determine the resulting droplet size distribution, the diluted pre-emulsion is filled in the pipe coil (d) after a steady state is reached and the pressure vessel valve is closed. The pre-emulsion is then processed by pressing it through the orifice. A sample of the resulting fine emulsion is collected from the hose (f) and analyzed using a laser light diffraction spectrometer including polarization intensity differential scattering (LS 13320® Beckman-Coulter, Brea, CA, USA). For process conditions without visible cavitation, a Thoma number of 0.3 is set by applying a backpressure with the needle valve (i). All process conditions are at least addressed three times if not specified otherwise. The software OriginPro 2019 (OriginLab Corp., Northampton, MA, USA) is used for the calculation of averages and standard deviations. Samples from three experiments were analyzed three times. Mean values are given with standard deviations.

3 Results

3.1 Cavitation Pattern

The flow is accelerated when entering the orifice due to the cross-section reduction. Resulting from the increased flow velocity, the static pressure in the orifice is decreasing. When the static pressure drops below the vapor pressure of the fluid, it partially vaporizes and cavitation bubbles are formed. These cavitation bubbles are then transported to the outlet channel of the orifices where they collapse as a result from the re-rising pressure due to decreasing velocity in the turbulent shear layer of the emerging free jet. It is expected that cavitation becomes more pronounced with increasing cavitation number σ.

Fig. 3 presents an overview of the cavitation pattern in the outlet channel at a pressure loss of 9.5 bar. The image is composed of two representative instantaneous pictures. In the presented inverted image areas with low dye concentration, representing areas with cavitation bubbles, are shown brighter. Areas with only liquid phase are presented in black. Cavitation bubbles outside the focus plane are depicted blurry. Areas close to the wall ($y/D < -3$ and $y/D > 3$) are colored gray due to the uneven distribution of the laser light in the edge region of the circular field of view.

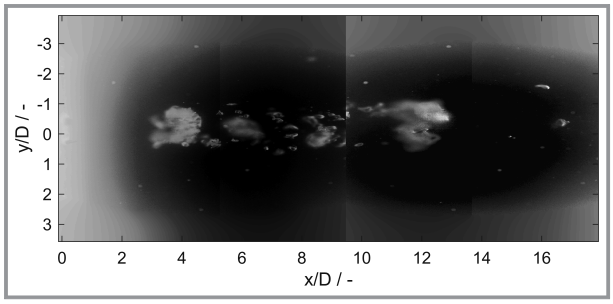

Figure 3. Cavitation pattern at $\Delta p = 9.5$ bar with $\sigma = 17$, $Th = 0.057$, and $Re = 916 \cdot 10^1$. Two representative instantaneous images are superimposed.

It is apparent from Fig. 3 that even at this low pressure loss, cavitation bubbles are created and transported downstream into the free jet. Single cavitation bubbles can be distinguished in a size range from about 20 µm to 200 µm. Cavitation bubbles were found exclusively at a distance of $x/D < 15$. The found cavitation pattern can be described as cavitation inception.

Fig. 4 shows the cavitation pattern in the outlet channel at a pressure loss of 19.5 bar. The image was composed of five representative instantaneous images. From Fig. 4, it is apparent that cavitation was more pronounced compared to a pressure loss of 9.5 bar. The cavitation bubbles left the orifice in large cavitation structures, which on some images are interrupted by areas with liquid only. Under these conditions, no stationary cavitation bubble ring surrounding the core region of the free jet was formed. The cavitation

 © 2021 The Authors. Chemie Ingenieur Technik published by Wiley-VCH GmbH

15222640, 2022, 3, Downloaded from https://onlinelibrary.wiley.com/doi/10.1002/cite.202100104 by Karlsruher Inst F. Technologie, Wiley Online Library on [21/10/2022]. See the Terms and Conditions (https://onlinelibrary.wiley.com/terms-and-conditions) on Wiley Online Library for rules of use; OA articles are governed by the applicable Creative Commons License

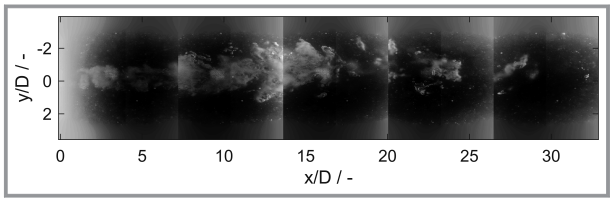

Figure 4. Cavitation pattern at Δp = 19.5 bar with σ = 36, Th = 0.028, and Re = 133 · 10^2. Five representative instantaneous pictures are superimposed.

bubbles were deformed in the subsequent mixing area of the free jet, where some bubbles even collapsed, as the visible number of cavitation bubbles decreased with growing distance from the orifice exit. The entrainment of the surrounding ambient fluid resulted in a spread of the jets and thus in a spread of the cavitation bubbles. Cavitation bubbles were found in the region of x/D < 30. The cavitation pattern changed from cavitation inception to jet cavitation.

The composed image in Fig. 5 shows the cavitation pattern at a pressure loss of 29.5 bar. As in Fig. 4, the image is composed of five instantaneous images. In general, the single images had a small contrast and seemed turbid. It is probable that the applied emulsifier stabilized small cavitation bubbles, as described in [33, 34], which are trapped in the backflow area surrounding the free jet. These small bubbles possibly resulted in a distortion of the emitted laser light. This distortion impeded the distinction between vapor and liquid phase far downstream the orifice exit. The brighter circular object in the center of every instantaneous image was caused by a malfunction of the camera sensor.

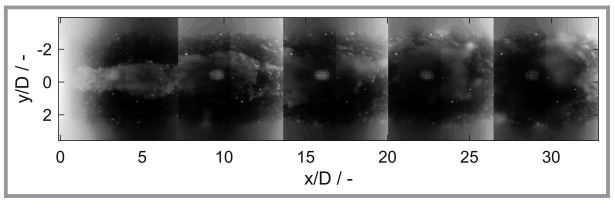

Figure 5. Cavitation pattern at Δp = 29.5 bar with σ = 54, Th = 0.019, and Re = 166 · 10^2. Five representative instantaneous pictures are superimposed.

In contrast to Fig. 4, a coherent cavitation jet was present at the outlet of the orifice. Large cavitation bubble clouds were found up to a distance of x/D < 25, giving the impression of pulsating cavitation. As with the previous experiment setup, the resulting cavitation pattern corresponds to jet cavitation.

A pressure loss of 49.6 bar resulted in the composed image of Fig. 6. When comparing Fig. 6 and Fig. 5, it can be noticed that the cavitation patterns show very high similarity. In both cases a coherent cavitation jet was present at the orifice exit. The free jet and thus the cavitation jet meandered to a higher extent compared to the conditions in Fig. 5. In addition, less distinct cavitation bubbles can be identified. The present cavitation pattern can again be described as jet cavitation.

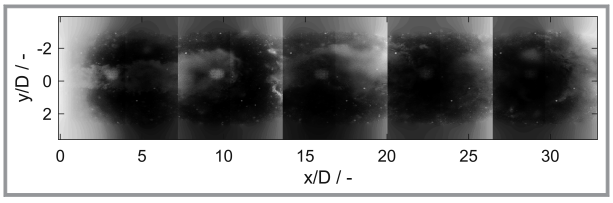

Figure 6. Cavitation pattern at Δp = 49.6 bar with σ = 92, Th = 0.011, and Re = 313 · 10^2. Five representative instantaneous pictures are superimposed.

Overall, the results indicate that even at small pressure losses cavitation is present in the flow. Furthermore, it can be confirmed that the cavitation intensity increases with an increasing pressure loss in the used system. It was not possible to achieve a hydraulic flip, as the limit of pressure stability of the optical accessible setup was reached.

3.2 Droplet Size Distributions

According to [15], larger droplets are found for σ > 2 (Th ≤ 0.31) corresponding to a cavitating flow. To verify this at the investigated process conditions, the droplet size distributions of samples, which were collected under conditions with and without cavitation, were determined. It is expected that larger median diameters are achieved when cavitation is present in the flow.

The resulting median diameters at the used pressure losses are presented in Fig. 7. For a cavitating flow (σ > 16) a median droplet size of 3.5 µm was found at a pressure loss of 9.5 bar. By further increasing the pressure loss, the resulting median droplet size decreases to 2 µm at a pressure loss of about 50 bar. When applying a backpressure and suppressing cavitation (σ > 25), a median droplet size of 3 µm was found at a pressure loss of 9.5 bar. Similar to the cavitating flow, the median droplet size decreases when the

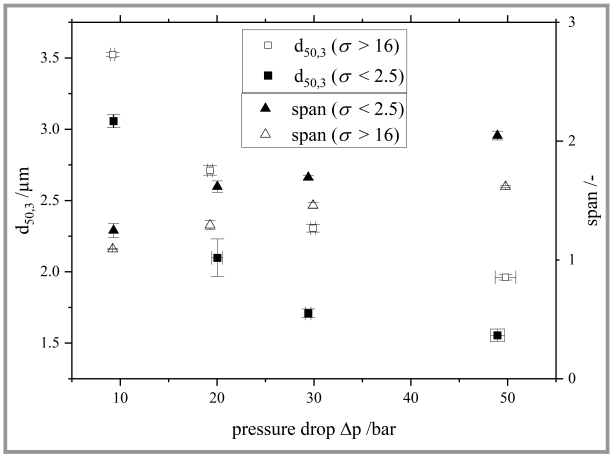

Figure 7. Resulting median droplet size $d_{50,3}$ (square symbols) and span (triangle symbols) in a cavitating (σ > 16, filled symbols) and in a cavitation-free flow (σ < 2.5, hollow symbols).

 © 2021 The Authors. Chemie Ingenieur Technik published by Wiley-VCH GmbH

15222640, 2022, 3, Downloaded from https://onlinelibrary.wiley.com/doi/10.1002/cite.202100104 by Karlsruher Inst F. Technologie, Wiley Online Library on [21/10/2022]. See the Terms and Conditions (https://onlinelibrary.wiley.com/terms-and-conditions) on Wiley Online Library for rules of use; OA articles are governed by the applicable Creative Commons License

pressure loss is increased with applied backpressure. A pressure loss of 50 bar with applied backpressure resulted in a median droplet size of 1.5 µm.

Furthermore, the resulting span of the droplet size distributions is depicted in Fig. 7. The span is calculated according to Eq. (5).

$$span = \left(d_{90,3} - d_{10,3}\right)/d_{50,3} \tag{5}$$

At a pressure loss of about 9.2 bar a span of 1.25 was found in the cavitation-free flow ($\sigma > 2.5$). The cavitation flow ($\sigma > 16$) at a pressure loss of 9.3 bar resulted in a span of 1.09. At both flow regimes, the span is increasing with increasing pressure loss and the cavitation-free flow always resulted in higher span values. Furthermore, the absolute difference of the span value between a cavitating flow and a cavitation-free flow is increasing with increasing pressure loss.

Since a change in the resulting droplet size distributions was found at all used process conditions when suppressing cavitation, it is hypothesized that cavitating flows lead to changes in the droplet deformation and breakup behavior at the corresponding process conditions.

3.3 Droplet Deformation and Breakup Visualization

Droplets are exposed to shear stress and elongational strain at the inlet of the orifice, causing a deformation of the droplets to thin threads when leaving the orifice. When the deformed droplets enter the turbulent shear layer of the emerging free jet, they are finally broken up due to the turbulent forces acting on them. The droplet breakup takes place stochastically in a specific area depending on the droplet trajectory and the vortex structure. It is hypothesized that the droplets in cavitating flow break up in a larger distance from the orifice exit, as the cavitation bubbles will influence the formation of the turbulent shear layer.

Fig. 8 presents the superimposition of many droplets in the outlet channel at a pressure loss of 9.5 bar without applied backpressure (a) and with applied backpressure (b) to illustrate the area of droplet breakup. Representative deformed single droplets and their temporal development are highlighted and enlarged. The droplet in the first frame of each double frame image is shown in gray while the droplets in the second frame, which was taken 10 µs later, is depicted black. Spherical and blurred droplets located in the backflow area surrounding the free jet are not portrayed for better visibility. The darker a place appears the more droplets were found at this place. Deformed droplets were found in the region of $0 \leq x/D \leq 15$ if cavitation was present ($\sigma = 17$). Even shortly behind the orifice exit, the droplets are deformed to complex basket-like shapes (see Fig. 8a1, a2), since, due to the high turbulent flow, the core region of the free jet is short [35, 36]. Thus, the droplets enter the shear layer soon, which causes the complex deformation. The numerous ring-like objects surrounding the jet are probably cavitation

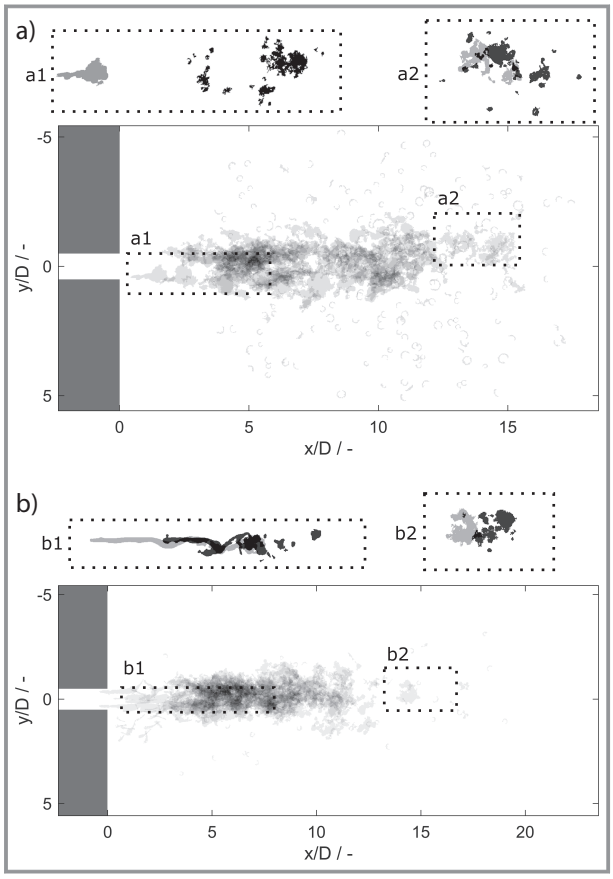

Figure 8. Droplet breakup at $\Delta p \approx 9.5$ bar: a) without backpressure ($\sigma = 17$, $Re = 916 \cdot 10^1$); b) with backpressure ($\sigma = 2.2$, $Re = 973 \cdot 10^1$).

bubbles that reflect the light of the droplets and are therefore detected as objects.

With applied backpressure (cavitation number of $\sigma = 2.2$, depicted in Fig. 8b), deformed droplets were found from $x/D \geq 0$ to $x/D \leq 15$. The small and thin deformed droplets in the area of $x/D = 1$ and $y/D = 2$ might either be droplets from the backflow, which are re-entrained in the jet as described in [3] or they might be caused by image errors such as reflections.

As a first tendency it can be found that larger droplets were visible in the region $x/D \geq 10$ if cavitation was present in the flow ($\sigma = 17$). The end of the droplet breakup region in the cavitating flow, which is here defined as the distance where the last big droplet was found, did not change however in the cavitation inception regime compared to the cavitation-free flow.

Fig. 9 shows deformed and broken droplets at a pressure loss of 19.5 bar without applied backpressure (a) and with applied backpressure (b). Droplets were detected in the range of $0 \leq x/D \leq 16$ when there was cavitation present ($\sigma = 35$, Fig. 9a). With applied backpressure ($\sigma = 2.2$, Fig. 9b), deformed droplets were only found in the area of $4 \leq x/D \leq 12$. Individual small droplets could be found up

 © 2021 The Authors. Chemie Ingenieur Technik published by Wiley-VCH GmbH

15222640, 2022, 3, Downloaded from https://onlinelibrary.wiley.com/doi/10.1002/cite.202100104 by Karlsruher Inst F. Technologie, Wiley Online Library on [21/10/2022]. See the Terms and Conditions (https://onlinelibrary.wiley.com/terms-and-conditions) on Wiley Online Library for rules of use; OA articles are governed by the applicable Creative Commons License

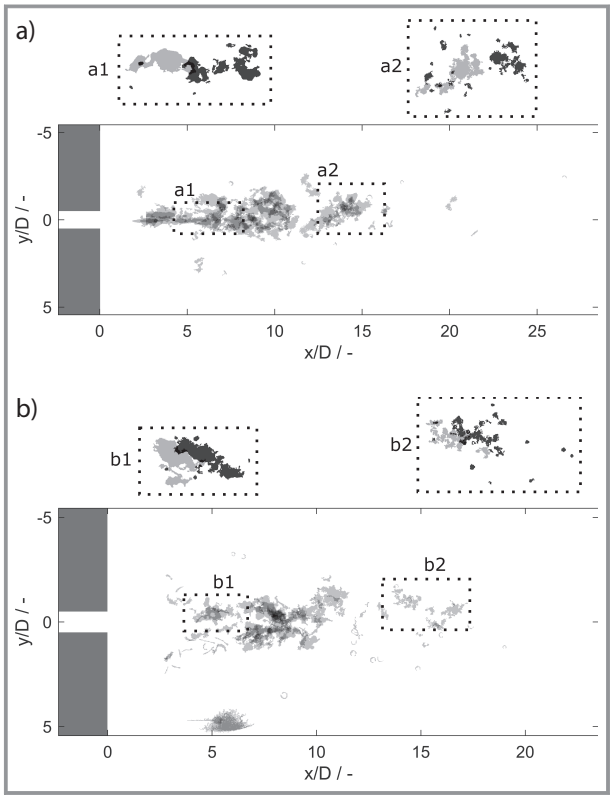

Figure 9. Droplet breakup at $\Delta p \approx 19.5$ bar: a) without backpressure ($\sigma = 35$, $Re = 133 \cdot 10^2$); b) with backpressure ($\sigma = 2.2$, $Re = 142 \cdot 10^2$).

to distance of $x/D = 15$. No difference in the droplet shape prior to their breakup was found when comparing deformed droplets in cavitating (Fig. 9a1) or non-cavitating flow (Fig. 9b1), respectively.

The superimposition of droplets passing the orifice at a pressure loss of 29.5 bar without backpressure (a) and with backpressure (b) can be compared in Fig. 10. Deformed droplets were found in the region of $4 \leq x/D \leq 15$ with applied backpressure ($\sigma = 2.2$, Fig. 10b). An individual larger droplet was found at a distance of $x/D = 17$. When turning to the droplet breakup within the cavitating flow at a pressure loss of 49.5 bar ($\sigma = 54$, Fig. 10a), it can be noticed that droplets were found in the area $4 \leq x/D \leq 22$. More and tending larger droplets were detected within the cavitating flow in the region $x/D > 15$ compared to the cavitation-free flow.

As shown in Fig. 11b, droplets were detected in the area of $0 \leq x/D \leq 17$ at a pressure loss of 49.5 bar with applied backpressure ($\sigma = 2.5$) and thus suppressed cavitation. When looking at the droplets in Fig. 11a at equal process conditions but without applied backpressure ($\sigma = 89$), it can be noticed that droplets were present in the area of $0 \leq x/D \leq 24$. Furthermore, only larger droplets were found when cavitation was present, since the high number of cavitation bubbles impeded the droplet visualization by distorting the emitted light of the droplets. Therefore, small droplets were too blurry to be detected as objects during the image processing.

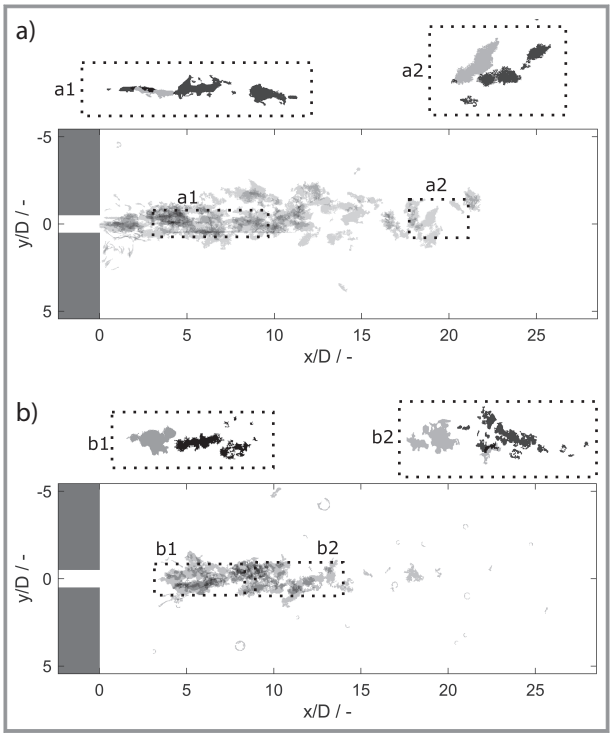

Figure 10. Droplet breakup at $\Delta p \approx 29.5$ bar: a) without backpressure ($\sigma = 54$, $Re = 165 \cdot 10^2$); b) with backpressure ($\sigma = 2.2$, $Re = 185 \cdot 10^2$).

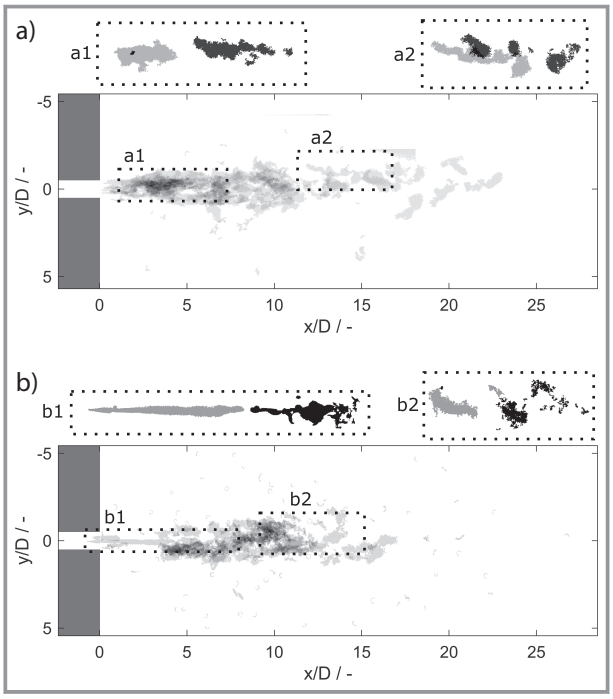

Figure 11. Droplet breakup at $\Delta p \approx 49.5$ bar: a) without backpressure ($\sigma = 89$, $Re = 247 \cdot 10^2$); (b) with backpressure ($\sigma = 2.5$, $Re = 383 \cdot 10^2$).

 © 2021 The Authors. Chemie Ingenieur Technik published by Wiley-VCH GmbH

15222640, 2022, 3, Downloaded from https://onlinelibrary.wiley.com/doi/10.1002/cite.202100104 by Karlsruher Inst F. Technologie, Wiley Online Library on [21/10/2022]. See the Terms and Conditions (https://onlinelibrary.wiley.com/terms-and-conditions) on Wiley Online Library for rules of use; OA articles are governed by the applicable Creative Commons License

4 Discussion

The results of this study show that even at low pressure losses cavitation was found in high-pressure homogenization when working without back-pressure ($Th \ll 0.3$). Depending on the pressure loss, two cavitation regimes were identified, namely cavitation inception for $\Delta p = 10$ bar and jet cavitation for $\Delta p \geq 20$ bar. No change in the cavitation regime was found when increasing the pressure loss from 30 bar to 50 bar. Presumably, a pressure loss of more than 100 bar is necessary to reach the choked cavitation regime as shown in [11], which could not be realized in the specific setup used in this study. Furthermore, it was found that no visible cavitation was present if a Thoma number of $Th = 0.3$ was set, which is consistent with the finding of Schlender et al. [15]. However, the cavitation inception still depends on the facility setup and the measurement technique [20]. In general, the onset of cavitation could be well described using the cavitation number σ, which is also expected to be the best method for predicting the onset of cavitation in a large-scale high-pressure homogenizer. When transferring the findings to an industrial scale high-pressure homogenizer, it has to be taken into account that the flow is induced by, e.g., piston pumps resulting in a pulsating flow, which leads to a stronger pulsating cavitation and thus in higher Reynolds stresses.

Emulsions of smaller median droplet sizes can be achieved if cavitation was suppressed by applying a back-pressure but keeping the total pressure loss constant, confirming the results of [15] even at low pressure losses. This allowed us to work with a specific optical accessible experimental setup. We could thus follow deformed droplets in the free jet and detect the location of their breakup.

At cavitation inception regime, no difference in the droplet breakup location was found compared to cavitation-free flow. However, a slight tendency of larger droplets at the end of the breakup area in a cavitating flow was noticed. Possibly, only some droplets interact with the cavitation bubbles and/or the flow field of the free jet is not much altered by the few cavitation bubbles. The tendency of a later droplet breakup in a cavitating flow is growing with an increasing pressure loss, and it is doing so with increasing cavitation intensity. For pronounced jet cavitation, the droplet breakup is completed further downstream. The change in the droplet breakup location can possibly be explained by the vortex weakening by cavitation as described by Ohta et al. [37] as well as the suppressed redistribution of the streamwise component of turbulence energy [38] in a shear layer. Although the vortex shedding frequency and thus the Reynolds stresses are increasing in cavitation flow [37], weaker vortexes may result in a smaller droplet deformation. Therefore, larger droplets can be found further downstream the orifice exit.

However, these findings may be somewhat affected by the fact that droplets were scaled to allow their visualization. The droplets in this study are relatively large in relation to the drilling hole of the orifice. In large-scale high-pressure homogenization processes, as the ones that are, e.g., applied in dairy industry, droplets are smaller by a factor of about 10. Therefore, droplets that pass a large-scale flat valve are expected to be less deformed. Furthermore, the ratio of the droplet size to the vortex sizes, as for example the Kolmogorov length-scale, is also larger in this study's setup compared to large scale high-pressure homogenization processes. Therefore, a droplet breakup in the turbulent inertia regime is more likely in this investigation [39, 40]. As the precise droplet breakup mechanism cannot be revealed, especially when cavitation is present, the influence of this mismatch on the findings cannot be determined. Nevertheless, as the location of the droplet breakup is mainly affected by the location and the intensity of the vortex structures in the shear layer, which is probably also affected in the large-scale process by the occurrence of cavitation, similar effects are expected in a large-scale process.

As it was not possible to properly visualize droplet breakup and cavitation bubbles at the same time, no statement on the interaction of droplets and cavitation bubbles can be made. Future research should focus on improving the applied visualization technique, especially the optical resolution.

5 Conclusions

The aim of this investigation was to examine the influence of a cavitating flow on droplet break during high-pressure homogenization.

This study has shown that the cavitation visualization technique presented by Gothsch et al. [16] for a microfluidic channel can also be applied at a coaxial high-pressure orifice. Cavitation inception and jet cavitation can be clearly distinguished. A limitation of this technique was that stabilized cavitation bubbles in the recirculation area of the free jet impeded the visualization at high cavitation intensities. Therefore, intense cavitation in the choked or hydraulic flip regime can presumably not be visualized with this technique in this geometry.

The experimental setup allowed following optically deformed droplets through the cavitating or non-cavitating free jets and analyzing their deformation and breakup. The experiments confirmed that smaller median droplets are achieved in cavitation-free flows compared to cavitation flows at same pressure loss (i.e., when the same specific energy is dissipated), even at low pressure drops and cavitation being not so pronounced as under industrial production conditions. However, differences in droplet breakup were only detected in the case of a pronounced jet cavitation regime. Here, droplet breakup takes place further downstream the orifice exit compared to a cavitation-free flow. This behavior increases with higher cavitation intensity. Nevertheless, a tendency of larger droplets at the end of the droplet breakup region was found at cavitation incep-

 © 2021 The Authors. Chemie Ingenieur Technik published by Wiley-VCH GmbH

15222640, 2022, 3, Downloaded from https://onlinelibrary.wiley.com/doi/10.1002/cite.202100104 by Karlsruher Inst F. Technologie, Wiley Online Library on [21/10/2022]. See the Terms and Conditions (https://onlinelibrary.wiley.com/terms-and-conditions) on Wiley Online Library for rules of use; OA articles are governed by the applicable Creative Commons License

tion, compared to cavitation-free flow. In order to understand the interaction of cavitation bubbles and emulsion droplets in more detail, considerably more work needs to be done using high-resolution optical measurement and simulation techniques.

The authors thank Dennis Scherhaufer and Heinz Lambach of the Institute for Micro Process Engineering (Micro Apparatus Engineering – FAB) for manufacturing of the orifice. We also thank Jürgen Kraft, Markus Fischer and Annette Berndt for their designing of the test site and assistance during the experiments. We thank Ralf Dorsner (wbk Institute of Production Science) for polishing the orifice. Furthermore, the authors thank the IOI Oleo GmbH for providing the oil. The authors also thank Peter Walzel for fruitful discussions on the concept of this study. We acknowledge financial support by the German Research Foundation (DFG), grant number 265685259.

Symbols used

c	[–]	circularity of the droplet
$crit$	[–]	threshold value for the droplet deformation
d	[µm]	droplet diameter
D	[mm]	dimensions of the orifice
e	[–]	extent of the droplet in the bounding box
L	[mm]	length of the orifice drilling hole
p	[bar]	pressure
Δp	[bar]	pressure loss
Re	[–]	Reynolds number
Th	[–]	Thoma number
$\bar{u}$	[m s^{-1}]	average velocity in the orifice
x	[µm]	x-direction
y	[µm]	y-direction
z	[µm]	z-direction

Greek letters

α	[°]	angle of the conical inlet
η	[Pa s]	dynamic viscosity
ρ	[kg m^{-3}]	density
σ	[–]	cavitation number

Sub- and Superscripts

bp	backpressure in the outlet channel
c	compensation
exit	outlet channel
in	inlet channel
v	vapor

References

[1] K. Kelemen, S. Gepperth, R. Koch, H.-J. Bauer, H. P. Schuchmann, *Microfluid Nanofluid* **2015**, *19 (5)*, 1139–1158. DOI: https://doi.org/10.1007/s10404-015-1631-z

[2] P. Walstra, P. E. A. Smulders, in *Modern Aspects of Emulsion Science* (Ed: B. P. Binks), Royal Society of Chemistry, Cambridge **1998**.

[3] F. J. Preiss, B. Mutsch, C. J. Kähler, H. P. Karbstein, *ChemEngineering* **2021**, *5 (1)*, 7. DOI: https://doi.org/10.3390/chemengineering5010007

[4] A. N. Kolmogorov, *Proc. R. Soc. Lond. A* **1991**, *434 (1890)*, 15–17. DOI: https://doi.org/10.1098/rspa.1991.0076

[5] A. N. Kolmogorov, *Proc. R. Soc. Lond. A* **1991**, *434 (1890)*, 9–13. DOI: https://doi.org/10.1098/rspa.1991.0075

[6] K. Kelemen, F. E. Crowther, C. Cierpka, L. L. Hecht, C. J. Kähler, H. P. Schuchmann, *Microfluid Nanofluid* **2015**, *18 (4)*, 599–612. DOI: https://doi.org/10.1007/s10404-014-1457-0

[7] M. Schlender, K. Minke, H. P. Schuchmann, *Chem. Eng. Sci.* **2016**, *142*, 1–11. DOI: https://doi.org/10.1016/j.ces.2015.11.028

[8] A. Philipp, W. Lauterborn, *J. Fluid Mech.* **1998**, *361*, 75–116. DOI: https://doi.org/10.1017/S0022112098008738

[9] A. Håkansson, *Annu. Rev. Food Sci. Technol.* **2019**, *10*, 239–258. DOI: https://doi.org/10.1146/annurev-food-032818-121501

[10] V. Gall, E. Rütten, H. P. Karbstein, *Exp. Comput. Multiphase Flow*, in press. DOI: https://doi.org/10.1007/s42757-020-0088-9

[11] M. Schlender, A. Spengler, H. P. Schuchmann, *Int. J. Multiphase Flow* **2015**, *74*, 84–95. DOI: https://doi.org/10.1016/j.ijmultiphaseflow.2015.04.004

[12] B. Freudig, S. Tesch, H. Schubert, *Eng. Life Sci.* **2003**, *3 (6)*, 266–270. DOI: https://doi.org/10.1002/elsc.200390042

[13] T. Gothsch, J. H. Finke, S. Beinert, C. Lesche, J. Schur, S. Büttgenbach, C. Müller-Goymann, A. Kwade, *Chem. Eng. Technol.* **2011**, *34 (3)*, 335–343. DOI: https://doi.org/10.1002/ceat.201000421

[14] C. C. Loo, W. L. Slatter, R. W. Powell, *J. Dairy Sci.* **1950**, *33 (10)*, 692–702. DOI: https://doi.org/10.3168/jds.S0022-0302(50)91958-8

[15] M. Schlender, K. Minke, B. Spiegel, H. P. Schuchmann, *Chem. Eng. Sci.* **2015**, *131*, 162–171. DOI: https://doi.org/10.1016/j.ces.2015.03.055

[16] T. Gothsch, C. Schilcher, C. Richter, S. Beinert, A. Dietzel, S. Büttgenbach, A. Kwade, *Microfluid Nanofluid* **2015**, *18 (1)*, 121–130. DOI: https://doi.org/10.1007/s10404-014-1419-6

[17] V. Gall, H. P. Karbstein, *ChemEngineering* **2020**, *4 (4)*, 64. DOI: https://doi.org/10.3390/chemengineering4040064

[18] A. Håkansson, L. Fuchs, F. Innings, J. Revstedt, B. Bergenståhl, C. Trägårdh, *J. Food Eng.* **2010**, *100 (3)*, 504–513. DOI: https://doi.org/10.1016/j.jfoodeng.2010.04.038

[19] F. Numachi, M. Yamabe, R. O-ba, *J. Basic Eng.* **1960**, *82 (1)*, 1–6. DOI: https://doi.org/10.1115/1.3662523

[20] E. P. Rood, *J. Fluids Eng.* **1991**, *113 (2)*, 163–175. DOI: https://doi.org/10.1115/1.2909476

[21] J.-P. Franc, J.-M. Michel, *Fundamentals of cavitation*, Springer science & Business media, Heidelberg **2006**.

[22] H. Soyama, Y. Yanauchi, K. Sato, T. Ikohagi, R. Oba, R. Oshima, *Exp. Thermal Fluid Sci.* **1996**, *12 (4)*, 411–416. DOI: https://doi.org/10.1016/0894-1777(95)00124-7

[23] A. Sou, S. Hosokawa, A. Tomiyama, *Int. J. Heat Mass Transfer* **2007**, *50 (17–18)*, 3575–3582. DOI: https://doi.org/10.1016/j.ijheatmasstransfer.2006.12.033

[24] Y. Yan, R. B. Thorpe, *Int. J. Multiphase Flow* **1990**, *16 (6)*, 1023–1045. DOI: https://doi.org/10.1016/0301-9322(90)90105-R

[25] A. A. McKillop, W. L. Dunkley, R. L. Brockmeyer, R. L. Perry, *J. Dairy Sci.* **1955**, *38 (3)*, 273–283. DOI: https://doi.org/10.3168/jds.S0022-0302(55)94971-7

 © 2021 The Authors. Chemie Ingenieur Technik published by Wiley-VCH GmbH

15222640, 2022, 3, Downloaded from https://onlinelibrary.wiley.com/doi/10.1002/cite.202100104 by Karlsruher Inst F. Technologie, Wiley Online Library on [21/10/2022]. See the Terms and Conditions (https://onlinelibrary.wiley.com/terms-and-conditions) on Wiley Online Library for rules of use; OA articles are governed by the applicable Creative Commons License

[26] S. Jahnke, in *Emulsions and nanosuspensions for the formulation of poorly soluble drugs: Based on the invited lectures and communications presented at the Colloidal Drug Carriers – 3rd Expert Meeting, Berlin* (Eds: R. H. Müller, S. Benita, B. H. I. Böhm), Medpharm Scientific Publ., Stuttgart **1998**.
[27] F. J. Preiss, T. Dagenbach, M. Fischer, H. P. Karbstein, *ChemEngineering* **2020**, *4 (4)*, 60. DOI: https://doi.org/10.3390/chemengineering4040060
[28] A. Bisten, D. Rudolf, H. P. Karbstein, *Microfluid Nanofluid* **2018**, *22 (5)*, 607. DOI: https://doi.org/10.1007/s10404-018-2076-y
[29] L. L. Hecht, A. Schoth, R. Muñoz-Espí, A. Javadi, K. Köhler, R. Miller, K. Landfester, H. P. Schuchmann, *Macromol. Chem. Phys.* **2013**, *214 (7)*, 812–823. DOI: https://doi.org/10.1002/macp.201200583
[30] P. Stephan, S. Kabelac, M. Kind, D. Mewes, K. Schaber, T. Wetzel, in *VDI-Wärmeatlas*, 12th ed., Springer Vieweg, Berlin **2019**.
[31] *CRC Handbook of Chemistry and Physics*, 84th ed. (Ed: D. R. Lide), CRC press, Boca Raton, FL **2003**.
[32] M. Tanaka, G. Girard, R. Davis, A. Peuto, N. Bignell, *Metrologia* **2001**, *38 (4)*, 301–309. DOI: https://doi.org/10.1088/0026-1394/38/4/3
[33] M. Schlender, *Untersuchungen zum Einfluss von strömungsinduzierter Kavitation auf den Emulgierprozess bei der Hochdruckhomogenisation*, Dissertation, Karlsruher Institut für Technologie (KIT) **2015**.
[34] J. Lee, T. Tuziuti, K. Yasui, S. Kentish, F. Grieser, M. Ashokkumar, Y. Iida, *J. Phys. Chem. C* **2007**, *111 (51)*, 19015–19023. DOI: https://doi.org/10.1021/jp075431j
[35] G. N. Abramovič, *The theory of turbulent jets*, M.I.T. Press, Cambridge, MA **1963**.
[36] N. Rajaratnam, *Turbulent jets*, Developments in water science, Vol. 5, Elsevier, Amsterdam **1976**.
[37] T. Ohta, H. Sakai, K. Okabayashi, T. Kajishima, *J. Fluid Sci. Technol.* **2011**, *6 (6)*, 1021–1035. DOI: https://doi.org/10.1299/jfst.6.1021
[38] T. Ohta, R. Sugiura, *J. Turbul.* **2019**, *20 (10)*, 599–625. DOI: https://doi.org/10.1080/14685248.2019.1685673
[39] N. Vankova, S. Tcholakova, N. D. Denkov, I. B. Ivanov, V. D. Vulchev, T. Danner, *J. Colloid Interface Sci.* **2007**, *312 (2)*, 363–380. DOI: https://doi.org/10.1016/j.jcis.2007.03.059
[40] A. N. Kolmogorov, *Dokl. Akad. Navk. SSSR* **1949**, *66*, 825–828.

 © 2021 The Authors. Chemie Ingenieur Technik published by Wiley-VCH GmbH

15222640, 2022, 3, Downloaded from https://onlinelibrary.wiley.com/doi/10.1002/cite.202100104 by Karlsruher Inst F. Technologie, Wiley Online Library on [21/10/2022]. See the Terms and Conditions (https://onlinelibrary.wiley.com/terms-and-conditions) on Wiley Online Library for rules of use; OA articles are governed by the applicable Creative Commons License